Document Version
Final published version

Licence
Dutch Copyright Act (Article 25fa)

Citation (APA)
Agbamu, D. O., Zhao, Q., Chen, C., Hajibeygi, H., & Ghanbarian, B. (2026). Theoretical modeling of hydrogen relative permeability relevant to underground hydrogen storage. *International Journal of Hydrogen Energy*, *202*, Article 152995. https://doi.org/10.1016/j.ijhydene.2025.152995

International Journal of Hydrogen Energy 202 (2026) 152995

Contents lists available at ScienceDirect

International Journal of Hydrogen Energy

journal homepage: www.elsevier.com/locate/he

Theoretical modeling of hydrogen relative permeability relevant to underground hydrogen storage

Deborah O. Agbamu [a], Qingqi Zhao [b], Cheng Chen [c], Hadi Hajibeygi [d], Behzad Ghanbarian [e,f,g,*]

[a] Porous Media Research Lab, Department of Geology, Kansas State University, Manhattan, 66506, KS, USA
[b] Stuttgart Center for Simulation Science (SC SimTech), University of Stuttgart, Universitätsstraße 32, 70569, Stuttgart, Germany
[c] Department of Civil, Environmental and Ocean Engineering, Stevens Institute of Technology, Hoboken, NJ, USA
[d] Faculty of Civil Engineering and Geosciences, Delft University of Technology, P.O. Box 5048, Delft, 2600, GA, the Netherlands
[e] iResearchE^3 Lab, Department of Earth and Environmental Sciences, University of Texas at Arlington, Arlington, 76019, TX, USA
[f] Department of Civil Engineering, University of Texas at Arlington, Arlington, 76019, TX, USA
[g] Division of Data Science, College of Science, University of Texas at Arlington, Arlington, 76019, TX, USA

ARTICLE INFO

Keywords:
Effective medium approximation
Percolation theory
Capillary pressure
Hydrogen relative permeability
Underground hydrogen storage

ABSTRACT

Underground hydrogen storage (UHS) is a potential technology that can resolve renewable energy supply-demand challenge at seasonal (terawatt-hours) scales. Enabling this technology and optimizing its performance require a wide range of analyses from hydrodynamics to geomechanics and biogeochemistry, among which understanding the transport (and trapping) of hydrogen in porous rocks stands out. A key parameter in quantification of hydrogen transport in partially brine-saturated geological formations is its relative permeability (k_{rh}). In this study, we develop a theoretical k_{rh} model using upscaling concepts from effective medium approximation and percolation theory. Our theoretical model, developed based on pore-scale characteristics, estimates k_{rh} from pore size distribution, capillary pressure curve or mercury intrusion capillary pressure curve, and critical hydrogen saturation, S_{hc}, at which k_{rh} approaches zero. We evaluate the proposed model using eight experimental datasets and eleven pore-network simulations. Discrepancies are observed for some of the carbonate samples, likely due to secondary porosity effects (e.g., presence of vugs and/or fractures), and in some of the sandstone rocks, possibly due to imprecise S_{hc} estimation. These observations highlight the importance of improving pore structure characterization to better account for such heterogeneities and enhance model accuracy for reliable quantification of the k_{rh} relevant to UHS applications. These findings also highlight the critical role of accurate parameter estimation, such as determining the S_{hc} in estimating k_{rh}. Overall, the study demonstrates that the proposed approach provides a cost-effective and practical alternative to extensive experiments and simulations, offering a promising tool for quantifying k_{rh} relevant to UHS applications.

1. Introduction

Underground hydrogen storage (UHS) is a viable method for storing large volumes of hydrogen, as hydrogen can be contained within subsurface structures, such as saline aquifers, depleted hydrocarbon reservoirs, and salt caverns [1]. It is also a key component of the "Power to Gas" concept in which surplus electricity is converted to hydrogen (H_2) via electrolysis [2], subsequently stored in underground reservoirs or injected into gas distribution networks, either directly through blending or additional conversion to methane. Various studies in the literature also highlight the expanding role of hydrogen in decarbonizing industry, advancing transport, and serving as a versatile energy carrier with high specific energy and strong potential for integration into future clean energy systems [3–5].

Although salt caverns offer high purity due to minimal contamination risk, their limited size and sparse availability may restrict their feasibility to meet extensive storage demands. In contrast, porous reservoirs offer significantly greater volumetric capacity. Furthermore, their operational costs are also substantially reduced since many sites already have existing exploration facilities [6,7]. Therefore, subsurface porous media, such as depleted hydrocarbon reservoirs and deep aquifers, provide feasible and abundant alternatives for long-term and

---

* Corresponding author. iResearchE^3 Lab, Department of Earth and Environmental Sciences, University of Texas at Arlington, Arlington, 76019, TX, USA.
E-mail address: ghanbarianb@uta.edu (B. Ghanbarian).

https://doi.org/10.1016/j.ijhydene.2025.152995
Received 27 June 2025; Received in revised form 29 November 2025; Accepted 9 December 2025

large-scale hydrogen storage [8,9].

Despite the growing interest in UHS, hydrogen storage mechanisms, including its transport and trapping, within subsurface heterogeneous porous media have not yet been fully understood. More specifically, quantification of the hydrogen flow characteristics, especially its relative permeability (k_{rh}), in the presence of existing in-situ fluids during injection is crucial to develop accurate large-scale models. Therefore, this study specifically investigates k_{rh}, a key parameter influencing hydrogen mobility and storage efficiency in subsurface porous media.

Relative permeability describes the ability of a fluid to flow within porous media in the presence of other immiscible fluids. In numerical modeling of UHS at the field scale, relative permeability curves are critical parameters, as highlighted by Bo et al. [10], Kanaani et al. [11], Lysyy et al. [12] and Wang et al. [13]. Laboratory-measured gas–water relative permeability curves typically show low endpoint gas saturations (<65 %) and *very low maximum gas relative permeabilities*, generally not exceeding 0.1 under drainage conditions [14–16], influenced by pore-scale heterogeneity, capillary number, low viscosity ratio of gas-brine systems, and injection rate [15–17]. Consequently, numerical and analytical models are essential for validating and extrapolating relative permeability data across broader saturation ranges [18,19]. This work aims to develop and evaluate a theoretical model for k_{rh} based on pore-scale characteristics, providing a cost-effective alternative to extensive laboratory measurements and simulations.

Direct pore-scale simulations have been applied to hydrogen–brine systems, demonstrating distinct saturation–permeability relationships for wetting and non-wetting phases and providing new insights into pore-scale controls on relative permeability [17]. While such simulations offer valuable pore-scale understanding, much of the historical development of relative permeability modeling has relied on simplified analytical formulations. One of the earliest models to predict relative permeability was developed by Corey [20] who derived relative permeability as a power-law function of normalized saturation. Although simple, the Corey model showed reasonable agreement with experimental data [20]. The Brooks-Corey model [21] expands upon this by introducing the concept of pore size distribution (PSD) in capillary pressure and relative permeability relationships, which improved predictions in water-wet reservoirs [22–24]. Along this line, van Genuchten [25] proposed a flexible and sigmoidal function to characterize capillary pressure curve, combined it with the hydraulic conductivity model of Mualem [26] and presented capillary pressure and relative permeability models. While effective in soil physics applications, similar to Brooks-Corey model [21], it is based on the bundle of capillary tubes approach, an oversimplifying idealization in which a porous medium with interconnected pores is replaced with non-interconnected straight capillary tubes [27]. Krevor et al. [18] modified the Brooks-Corey model [21] to improve CO_2 relative permeability by capturing capillary trapping behavior. Lenhard et al. [28] developed a method to derive equivalent parameters for the Brooks-Corey [21,25] and the van Genuchten [25] model. These models were applied and compared by Bo et al. [10] in their study on relative permeability of modelling of hydrogen who found that the Krevor et al. approach [18] had the best agreement with experimental data. Parker et al. [29] developed a semi-empirical model incorporating hysteresis and non-wetting phase entrapment to capture history-dependent multiphase flow. However, it remains reliant on empirical calibration and lacks explicit pore-scale representations, such as film flow and wettability effects. Ogolo et al. [30] emphasized the importance of laboratory-derived relative permeability data and demonstrated that even minor inaccuracies in the Corey model exponents can have considerable impacts on reservoir simulations. Their study underscores the necessity of precise calibration of these models to specific reservoir conditions to ensure accurate predictions.

In contrast to the bundle of capillary tubes approach, techniques from statistical physics, such as percolation theory (PT) [31,32] and effective medium approximation (EMA) [33], scale up flow and transport in complex pore networks with interconnected pores to model relative permeability in porous media [34–36]. For instance, Ghanbarian et al. [37] combined PT and EMA to model wetting-phase relative permeability in porous media. They applied scaling laws from EMA and PT respectively at higher and lower wetting-phase saturations. By comparison with experiments, they found generally good agreement with measurements. In another study, Ghanbarian et al. [38] applied a similar approach, adopted for unconventional reservoirs, and proposed a model for gas relative permeability in shales and tight rocks. Due to nano-scale pore structures of unconventional rocks, their model accounted for slippage. By comparing with six sets of experiments and two sets of simulations, Ghanbarian et al. [38] found accurate predictions of gas relative permeability.

Although concepts of PT and EMA have previously been used to model relative permeability in soils [37] and tight porous rocks [38], to the best of the authors' knowledge, this is the first study evaluating their applications to hydrogen in conventional reservoir rocks. We aim to advance the current understanding of hydrogen flow behavior through the following objectives: (1) upscaling pore-scale flow using the EMA and universal power-law scaling from PT, (2) modeling hydrogen relative permeability k_{rh} in porous rocks and (3) evaluating the proposed model and its predictions by comparison with numerical simulations and experimental measurements. The remainder of this paper is structured as follows: the theoretical framework and dataset are first described, followed by a presentation and discussion of the results. The paper concludes with a summary of the main findings.

2. Theoretical modeling of hydrogen relative permeability

In this section, we present the theoretical approach developed to model the $\boldsymbol{k_{rh}}$.

2.1. Hydraulic properties at the pore scale

For a cylindrical pore, the Young-Laplace equation relates the pore size to the capillary pressure as

$$r = \frac{2\gamma\cos(\theta)}{P_c}, \tag{1}$$

where r is the pore radius, γ is the interfacial tension (N/m) between the two immiscible fluids (e.g., mercury-air or water-hydrogen), θ is the contact angle (°) between fluid and solid surface, and P_c is the capillary pressure (Pa), defined as the pressure difference between the non-wetting and wetting phases (hydrogen gas and brine, respectively).

Hagen-Poiseuille's law describes viscous flow in a cylindrical pore, where the volumetric flow rate is proportional to the pore radius raised to the fourth power. Based on the Hagen-Poiseuille model the hydraulic conductance, g (m^4s/kg), of fluid flow through a cylindrical pore with length l, filled with fluid of viscosity μ, is given by

$$g = \frac{\pi r^4}{8\mu l} \tag{2}$$

Based on Equation (2) and the relationship between g and r, one can determine the pore conductance distribution, $f(g)$, from the PSD and the relationship $f(g) = f(r)dr/dg$ in which $f(r)$ represents the PSD.

2.2. Hydrogen saturation

We assume that the pore space can be represented by a network of cylindrical pores whose lengths are proportional to their radii. Each pore is occupied by either wetting (e.g., water) or non-wetting (e.g., hydrogen) fluid, and all pores with radius r and larger are considered accessible to hydrogen. The hydrogen saturation S_h associated with a given pore radius r can then be determined by integrating $r^3 f(r)$ from r to r_{max} and normalizing the results as follows [38]

$$\frac{S_h - S_{hr}}{1 - S_{hr}} = \frac{\int_r^{r_{max}} r^3 f(r)dr}{\int_{r_{min}}^{r_{max}} r^3 f(r)dr} \tag{3}$$

where S_{hr} is the residual hydrogen saturation and $f(r)$ is the pore size distribution.

2.3. *Upscaling from pore to core*

To model k_{rh} over the entire S_h range from the critical hydrogen saturation, S_{hc}, at which hydrogen permeability approaches zero [32], to 1, we apply the EMA at high to intermediate S_h and PT at low S_h near S_{hc}. In the following, we briefly describe the EMA and PT and scaling laws used to model k_{rh}.

The EMA is an upscaling technique from statistical physics, which provides a method for modeling flow and transport in porous materials. This approach has been effectively employed in the literature to study various petrophysical properties by Ghanbarian et al. [38], Ghanbarian & Javadpour [39], and Richesson & Sahimi [40]. Within the EMA framework, a heterogeneous medium characterized by a given pore conductance distribution $f(g)$ is substituted with a hypothetically homogeneous network where all pores possess an effective pore conductance g_e. This effective pore conductance g_e, is determined by solving [54]

$$\int \frac{g_e - g}{g + \left[\frac{Z}{2} - 1\right] g_e} f(g)dg = 0, \tag{4}$$

in which Z is the average pore coordination number. Assuming $Z = 2/S_{hc}$, according to the literature [38], one can rewrite Equation (4) as

$$\int \frac{g_e - g}{g + \left[\frac{1-S_{hc}}{S_{hc}}\right] g_e} f(g)dg = 0. \tag{5}$$

Equation (5) means that the effective hydrogen conductance, g_e, at the network level can be scaled up from pore-scale properties using the pore size distribution and S_{hc}.

Under the fully-saturated conditions ($S_h = 1$), the effective conductance g_e is determined by integrating the conductance distribution as

$$\int_{g_{min}}^{g_{max}} \frac{g_e(S_h = 1) - g}{g + \left[\frac{1-S_{hc}}{S_{hc}}\right] g_e(S_h = 1)} f(g)dg = 0. \tag{6}$$

Under the partial saturation conditions, one obtains

$$\int_{g_{min}}^{g} \frac{g_e(S_h) - 0}{0 + \left[\frac{1-S_{hc}}{S_{hc}}\right] g_e(S_h)} f(g)dg + \int_{g}^{g_{max}} \frac{g_e(S_h) - g}{g + \left[\frac{1-S_{hc}}{S_{hc}}\right] g_e(S_h)} f(g)dg = 0. \tag{7}$$

The values of $g_e(S_h = 1)$ and $g_e(S_h)$ should be determined by numerically solving Equations (6) and (7), respectively. To characterize the saturation dependence of the effective conductance, $g_e(S_h)$ should be computed at different S_h values. One can accordingly calculate the k_{rh}, following [35], as

$$k_{rh} = \frac{k_h(S_h)}{k_h(S_h = 1)} = \frac{g_e(S_h)}{g_e(S_h = 1)}. \tag{8}$$

Predictions by the EMA are accurate far above S_{hc} [41]. Therefore near S_{hc}, one should apply another upscaling technique e.g., universal power-law scaling from PT. The universal power-law scaling from PT [33] is

$$k_{rh} = k_0(S_h - S_{hc})^t, S_h > S_{hc}, \tag{9}$$

where t is the scaling exponent whose universal value is dimension-dependent (1.3 for two and 2 for three dimensions). k_0 is a numerical prefactor that can be determined by equating Equations (8) and (9) at S_{hx}, the crossover point between the EMA and the universal power-law scaling from PT.

Because Eq. (8) is expressed implicitly in terms of S_h, one should numerically determine k_0 and S_{hx}. The procedure involves interpolating the estimated k_{rh} values over a range of hydrogen saturations between S_{hc} and 1, for example using a spline method, followed by calculating k_0 and the slope at each point. The value of S_{hx} is then identified as the hydrogen saturation at which the values of k_{rh} determined by Eqs. (8) and (9) are equal and the difference in their slopes become minimal. For samples with relatively high S_{hc}, a smooth crossover may not exist. In such cases, S_{hx} is selected as the saturation where the slope difference between the two equations is minimized. This behavior may lead to an abrupt transition from the PT scaling to the EMA scaling.

The Python source code used in this study to estimate the k_{rh} curve from either the H_2-brine capillary pressure curve (CPC), mercury intrusion capillary pressure (MICP) or PSD is available at HydroShare [42].

Eq. (9) with exponent $t = 2$ was originally proposed to describe flow and model conductivity in three-dimensional homogeneous lattices composed of bonds with identical conductance [33]. However, when the PSD of a rock sample is sufficiently narrow, Eq. (9) is expected to provide accurate estimations of k_{rh} across the full range of hydrogen saturation from S_{gc} to 1, as demonstrated in Section 4.

3. Methods and data

The data used in this study to evaluate our k_{rh} model consist of eight experiments and eleven pore-network models (PNMs). Salient properties of each dataset are summarized in Table 1. The H_2-brine drainage CPC, MICP or both measurements were available in all datasets except Manoorkar et al. [16] where only the PSD was reported. In what follows, we briefly describe each dataset. Interested readers are referred to the original publications for further details.

3.1. *Experiments*

3.1.1. *Yekta et al. Dataset*

In the Yekta et al. [43] study, a Triassic sandstone sample from the Buntsandstein Formation in France was tested for UHS application. Capillary pressure and relative permeability experiments were conducted under simulated shallow (20°C and 55 bar) and deep (45°C and 100 bar) reservoir conditions. For both conditions, the value of porosity was equal to 0.19 (Table 1), measured via mercury intrusion porosimetry. Water saturation measurements utilized the mass balance method. A modified semi-dynamic technique combined with the MICP method was utilized to derive CPC evolution for the H_2–water system over the entire water saturation range. The interfacial tension (IFT) values (0.051 N/m for shallow and 0.046 N/m for deep reservoir condition) and contact angles ($\cos(\theta) = 0.93$ for shallow and 0.82 for deep reservoir condition) for the hydrogen–water system were determined under UHS condition.

The k_{rh} was determined using the conventional steady-state approach. It was not possible to decrease the water saturation below 40 % during the experiment. Therefore, Yekta et al. [43] extended the data to lower saturations using P_c measurements from the core-flooding experiments. For the purpose of our study, PSD was derived from the H_2-brine CPC data and MICP data obtained from the same sample.

3.1.2. *Rezaei et al. Dataset*

In this dataset, Rezaei et al. [45] conducted displacement tests on two sandstones (S1 and S2) and one carbonate (C1) rock core samples from gas reservoirs. The mineralogy and pore structure of the samples were analyzed through the XRD analysis, MICP experiments, and a centrifuge P_c test. Experiments were carried out to measure the relative permeability of hydrogen and brine under various conditions to investigate the impacts of pressure, salinity, rock type (sandstone and

Table 1
Information on the nineteen datasets used in this study.

Reference	Sample	Remarks	Porosity (%)	Capillary Pressure		PSD	Simulation	Experiment
				CPC	MICP			
Yekta et al. [43]	Buntsandstein Sandstone	Shallow	19	✓	✓	✗	✗	Steady-state
		Deep	19	✓		✗	✗	Steady-state
Hashemi et al. [44]	Berea[a]	Berea	18	✓	✗	✗	PNM	✗
	Berea	Berea (small)	20	✓	✗	✗	PNM	✗
	A1	Sandstone	43	✓	✗	✗	PNM	✗
	C1	Carbonate	25	✓	✗	✗	PNM	✗
	C2	Carbonate	16	✓	✗	✗	PNM	✗
Rezaei et al. [45]	S1	Sandstone	16	✗	✓	✗	✗	Unsteady state
	S2	Sandstone	11	✗	✓	✗	✗	Unsteady state
	C1	Carbonate	13	✗	✓	✗	✗	Unsteady state
Boon & Hajibeygi [14]	Berea	Sandstone	20	✓	✓	✗	✗	Steady-state
Higgs et al. [15]	Bentheimer	Sandstone	23	✗	✓	✓	✗	Steady-state
Zhao et al. [46]	S1 SCA	Sandstone	25	✓	✗	✗	PNM	✗
	S1 LCA	Sandstone	25	✓	✗	✗	PNM	✗
	S2	Sandstone	17	✓	✗	✗	PNM	✗
	S3	Sandstone	17	✓	✗	✗	PNM	✗
	S7	Sandstone	34	✓	✗	✗	PNM	✗
	BG	Bandera Gray sandstone	21	✓	✗	✗	PNM	✗
Manoorkar et al. [16]	Carbonate	Fractured rock	1	✗	✗	✓	✗	Steady-state

[a] Represents the base-case from the literature [44].

carbonate), and gas type (H_2, N_2, and CH_4). Those authors conducted five sets of experiments (Exp 1–5) on the S1 core sample. In the first three, the backpressure was varied (0.1, 10.34, and 20.68 MPa) while maintaining a constant brine salinity of 35 ppt (parts per thousand). In the remaining two experiments, the salinity was varied (100 and 200 ppt) under a constant backpressure of 20.68 MPa. For the S2 core sample, three experiments were performed, each using a different gas (H_2, N_2, and CH_4) at a fixed pressure of 20.68 MPa and a salinity of 35 ppt. The C1 core sample was tested using only hydrogen under the same pressure and salinity conditions (20.68 MPa and 35 ppt). In our study, we focused exclusively on the hydrogen experiments from each core sample, and our modeling results were compared against these hydrogen-specific measurements to assess performance.

3.1.3. *Boon and Hajibeygi dataset*

Boon and Hajibeygi [14] investigated H_2-water flow in a heterogeneous Berea sandstone under both drainage and imbibition conditions. Steady-state drainage and imbibition core-flooding experiments were performed, and the transport of hydrogen and water was visualized using X-ray imaging. We, however, used only the drainage data to evaluate our model as there was no CPC for the imbibition process. P_c measurements were combined with MICP data to derive a receding contact angle for the H_2/water/sandstone system. To extend the CPC over the full saturation range and determine the receding contact angle of the H_2-brine system, Boon and Hajibeygi [14] combined H_2-brine P_c measurements with MICP data from a Berea sandstone core of comparable porosity and permeability, as reported by Ni et al. [47].

3.1.4. *Higgs et al. Dataset*

Higgs et al. [15] measured k_{rh} hysteresis during co-injection core floods of hydrogen and water in a Bentheimer sandstone. The core sample used in their study had a porosity of 23% and absolute permeability of 653 mD. Experiments were carried out at 298°K and 2.133 MPa with hydrogen viscosity of 0.00891 mPa.s and density of 1.7141 kg/m^3. Experimental procedures involved two pumps which injected deionized water and pure hydrogen into a flowline, with pressure measured using transducers. The confining pressure was maintained at 6.21 MPa, while pore pressure was constrained close to 2.13 MPa using a back pressure regulator. The fractional flow of hydrogen was incrementally increased to determine irreducible water saturation and subsequently decreased to determine residual gas saturation. Relative permeability for water and hydrogen was determined as a function of saturation. MICP was used to determine $P_c - S$ relationship of the Bentheimer sandstone. Micro-CT images were employed by those authors to determine fluid saturations and pore size distribution. For our study, PSD from MICP and CT image was used. In this study, we used the MICP and micro-CT–derived pore-size distributions to estimate hydrogen–water relative permeabilities with the EMA model described in Section 2.3, and we compared these estimated curves with the drainage and imbibition relative permeabilities measured by Higgs et al. (Fig. 4c).

3.1.5. *Manoorkar et al. Dataset*

In their study, Manoorkar et al. [16], experimentally measured the relative permeability of hydrogen, methane, and nitrogen in a fractured carbonate reservoir rock. Using steady-state experiments at 10 MPa on a cylindrical core from the Loenhout natural gas storage site in Belgium, they measured gas-brine flow behavior and phase interference within μm-to-mm scale fractures. Those authors obtained the aperture distribution from segmented dry scans. The specific modeling treatment of this fractured carbonate sample, including the use of fracture aperture distributions and cubic-law-based conductance, is described in Section 3.3.

3.2. *Numerical simulations*

3.2.1. *Hashemi et al. Dataset*

Hashemi et al. [44] investigated H_2-brine multiphase flow at the pore scale using quasi-static pore network modeling (PNM) and simulated CPC and relative permeabilities. They established a base case by matching their simulation with experiment conducted by Yekta et al. [43] under shallow aquifer conditions. They studied cyclic hysteretic multiphase flow and investigated sensitivities to contact angles ($51^{\circ} \leq \theta \leq 83^{\circ}$) and rock structure (sandstones and carbonates). We note that Hashemi et al. [44] developed their models using the Yekta et al. [43] dataset as a base case, so these two datasets are closely related. More specifically, CPCs of the five PNMs extracted from images of three sandstones (Berea*, Berea and A1) and two carbonates (C1 and C2) were used in our study.

3.2.2. *Zhao et al. Dataset*

Zhao et al. [46] studied k_{rh} under drainage and imbibition conditions in a H_2-brine-rock system. In our study, we used only the primary drainage data because the P_c measured under imbibition exhibited complexities, including negative values. Pore structural information was extracted from rock sample images to construct pore network models. They simulated CPCs and relative permeability curves for five sandstones (S1, S2, S3, S7 and Bandera Gray [BG]) with different structures. The influence of wettability was examined for S1 by varying the contact angle from 26.3° to 35.8° to represent different water-wet conditions during drainage. Then, the contact angle was fixed at 26.3° for the other samples to investigate the effects of other factors, such as pore connectivity and pore-to-throat diameter ratio. In our analysis, we derived PSD from the simulated CPC for all five sandstones, and the corresponding relative permeabilities were estimated. In our analysis, we use the primary drainage curves reported by Zhao et al. [46], while the corresponding petrophysical properties required for modeling are summarized in Table 1.

3.3. *Estimating k_{rh}*

In our study, we estimated k_{rh} from the S_{hc} and PSD using the studies contained in Table 1. The latter, if not available, was derived from either the CPC or MICP by plotting $\Delta S_w / \Delta \ln(P_c)$ against r. More specifically, Eq. (1) was used to determine the pore radius from the capillary pressure. To estimate the maximum pore radius r_{max}, we applied the Fredlund and Xing [48] method, fitted a tangent line at the inflection point of the CPC or MICP, and then extrapolated to the straight line corresponding to full water saturation ($S_w = 1$), following Zare Sourmanabad et al. [53]. The resulting entry pressure was accordingly used to calculate r_{max} via the Young-Laplace equation. This ensures that the PSD has a realistic upper limit, preventing artificial extension into unrealistically large pores and thereby improving the accuracy of flow modeling.

Following Ghanbarian-Alavijeh and Hunt [55] and Ghanbarian and Javadpour [39], the critical hydrogen saturation, S_{hc}, was estimated from the inflection point of the CPC or mercury intrusion porosimetry curve as $S_{hc} = 1 - S_{winf}$ where S_{winf} is the water saturation corresponding to the inflection point on the curve. The estimated values from the MICP and CPC are reported in Table 2. The S_{hc} values determined directly from the measured or simulated $S_h - k_{rh}$ curves (denoted as data-derived S_{hc} hereafter) are also given.

As explained in Section 2, k_{rh} was estimated using the EMA at high to intermediate S_h and PT at low S_h near S_{hc}. The saturation at which flow switches from PT to EMA is the crossover saturation denoted as S_{hx}. Recall that to calculate S_{hx}, we first interpolated the estimated k_{rh} values at various hydrogen saturations between S_{hc} and 1. We then calculated k_0 and the slope at each point. S_{hx} corresponds to the gas saturation at which the k_{rh} values determined by Equations (8) and (9) are equal and the difference between their slopes become minimal.

Capillary trapping was quantified by estimating the residual water saturation from the drainage H_2–brine CPC or MICP curves. The P_c above which no further water displacement occurs within pores was identified, and the corresponding water saturation was considered as the residual water saturation. Pores associated with this P_c and smaller were excluded from the model, as the water they contain does not actively participate in flow processes. Where this is not captured by CPC, we use the maximum S_h from the relative permeability measurement and set residual water saturation as $1 - S_h$.

In all datasets studied here except the Manoorkar et al. [16], we applied Hagen-Poiseuille's law. Accordingly, in Eq. (2) we set the hydraulic conductance of each pore throat proportional to r^4 thereby linking the pore size distribution to macroscopic transport properties through the EMA and PT. However, because Manoorkar et al. [16] studied fractures, we replaced the exponent 4 in Equation (2) with 3 based on Cubic law [49]. In datasets where both the CPC and MICP curves were available (i.e., Yekta et al. [43] and Boon and Hajibeygi [14]), we estimated the k_{rh} from both and compared them. The PSD from CT images was available alongside the MICP in the Higgs et al. [15] dataset and both were used to compute k_{rh}.

4. Results

In this section, we present the CPCs and PSDs in each dataset and then compare the k_{rh} curves estimated via the proposed model with the experiments and simulations.

4.1. *Comparison with experiments*

Fig. 1a and b shows the MICP and H_2-brine CPC as well as the derived PSD for the shallow-reservoir sample, and Fig. 1d and e exhibit them for the deep-reservoir sample from Yekta et al. [43]. The estimated k_{rh} curves from the H_2-brine CPC and MICP are presented in Fig. 1c and f for the shallow- and deep-reservoir samples, respectively. The H_2-brine CPCs (Fig. 1a and d) indicate that hydrogen displaces more water at higher P_c values, resulting in reduced water trapping, which is more pronounced than that in the MICP measurements (Fig. 1a and d).

Table 2

Critical hydrogen saturation (S_{hc}) values for the experiments and simulations analyzed in this study. We determined the S_{hc} value directly from experimental or simulated $k_{rh} - S_h$ data and estimated it from either the mercury intrusion porosimetry curve (MICP) and/or H_2-brine capillary pressure curve (CPC) for each dataset.

Dataset	Sample	Remarks	Porosity (%)	S_{hc} (Fractional)		
				Estimated from		Determined directly from **k_{rh}-S_h** data
				MICP	CPC	
Yekta et al. [43]	Buntsandstein Sandstone	Shallow	19	0.42	0.31	0.1
		Deep	19	0.42	0.44	0.18
Hashemi et al. [44]	Berea[a]	Berea	18	NAˆ[b]	0.2	0.2
	Berea	Berea (small)	20	NAˆ[b]	0.25	0.3
	A1	Sandstone	43	NAˆ[b]	0.2	0.2
	C1	Carbonate	25	NAˆ[b]	0.06	0.06
	C2	Carbonate	16	NAˆ[b]	0.35	0.35
Rezaei et al. [45]	S1	Sandstone	16	0.09	NAˆ[b]	0.0015
	S2	Sandstone	11	0.2	NAˆ[b]	0.009
	C1	Carbonate	13	0.15	NAˆ[b]	0.003
Boon & Hajibeygi [14]	Berea	Sandstone	20	0.31	0.4	0.04
Higgs et al. [15]	Bentheimer	Sandstone	23	0.46	NAˆ[b]	0.46
Zhao et al. [46]	S1 SCA	Sandstone	25	NAˆ[b]	0.31	0.06
	S1 LCA	Sandstone	25	NAˆ[b]	0.31	0.05
	S2	Sandstone	17	NAˆ[b]	0.25	0.6
	S3	Sandstone	17	NAˆ[b]	0.5	0.2
	S7	Sandstone	34	NAˆ[b]	0.36	0.13
	BG	Bandera Gray sandstone	21	NAˆ[b]	0.07	0.07
Manoorkar et al. [16]	Carbonate	Fractured rock	1	NAˆ[b]	NAˆ[b]	0.08

[a] Represents the base-case from the literature [44].

[b] indicates Not Available.

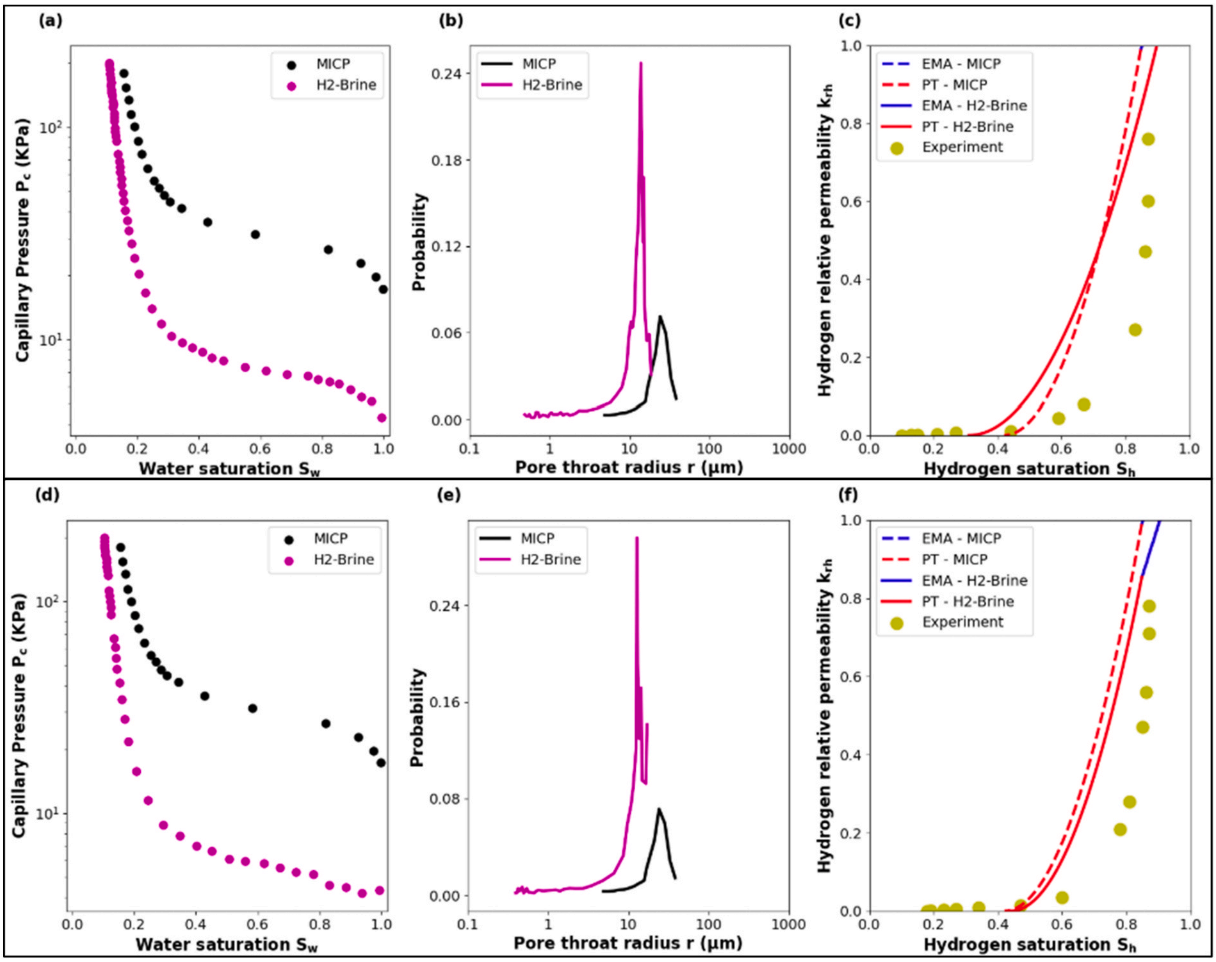

Fig. 1. (Left) CPC (a and d), (middle) PSDs (b and e), and (right) estimated and measured hydrogen relative permeability curves (c and f) for the Buntsandstein sandstone sample at (top) shallow and (bottom) deep reservoir conditions. Experimental data are from the Yekta et al. [43] study.

Additionally, hydrogen demonstrates a greater ability to penetrate smaller pore spaces (Fig. 1b and e), leading to a lower residual water saturation (Fig. 1a and d).

Fig. 2 presents the CPCs, PSDs, and k_{rh} curves for the sandstone samples S1 (Fig. 2a–c), S2 (Fig. 2d–f), and C1 (Fig. 2g–i) from Rezaei et al. [45]. Recall that only the MICP data are available for this dataset (Table 1). We did not estimate the residual water saturation from the MICP as it was not representative of the different conditions that were investigated by those authors. The residual water saturation was estimated by subtracting the maximum S_h observed from the $S_h - k_{rh}$ curves from 1. For S1, we averaged the residual water saturation over the five experiments (Exp 1–Exp 5).

The experiments 1–5 in Fig. 2c represent measurements conducted under different salinity and pressure conditions. For sample S1, we found good agreement between the estimated and measured k_{rh} curves (Fig. 2c). However, at very low S_h values, the model underestimated k_{rh}.

The MICP curve of the C1 carbonate sample (Fig. 2g) shows that higher capillary pressures were needed near full saturation to drain pores. The estimated k_{rh} for the C1 sample is shown in Fig. 2i. As can be observed, the proposed model underestimated the k_{rh} for $S_h < 0.2$ and overestimated its value for $S_h > 0.2$.

Fig. 3 presents the CPCs, PSDs, and k_{rh} curves for the Berea sandstone sample from Boon and Hajibeygi [14]. As illustrated in Fig. 3b, the PSDs obtained from the H_2-brine CPC and MICP measurements are extremely narrow, with the distribution from the former exhibiting the greatest constriction. The estimated k_{rh} from the MICP is shown via the dashed line and from the CPC via the solid line in Fig. 3c.

In Fig. 4a–c, we respectively illustrate the MICP curve, PSDs derived from the MICP and determined from CT image analysis and k_{rh} curves for the Bentheimer sandstone sample from Higgs et al. [15]. The PSD obtained from the MICP spans nearly one order of magnitude, similar to that derived from the micro-CT imaging (Fig. 4b) but did not capture as many smaller pores. The critical hydrogen saturation $S_{hc} = 0.46$, determined from the inflection point of the MICP curve, seems to agree well with the data-derived value of 0.46, determined from the measured k_{rh} curve (Table 2). As shown in Fig. 4c, the k_{rh} curve estimated from the micro CT-based PSD matched the experiments more accurately than that estimated from the MICP-based PSD.

Fig. 5a shows the aperture size distribution, derived from the CT images of the fractured carbonate sample from Manoorkar et al. [16]. The sample has very low matrix porosity (less than 0.01). Since neither the MICP nor the CPC data are available for this sample, we estimated the k_{rh} using the data-derived $S_{hc} = 0.08$, determined from the k_{rh} experimental measurements (Table 2).

Fig. 5b shows the estimated k_{rh}, depicted as line plots, and the measured k_{rh}, shown as dot plots, for the fractured carbonate sample. We found that the estimated curve agreed with the measured one at low S_h values reasonably well. For this dataset, the exponent 4 in Equation (2) was replaced with 3, according to the cubic law.

4.2. Comparisons with simulations

Fig. 6 presents the results for three sandstone (Fig. 6a–i) and two carbonate samples (Fig. 6j–o) from Hashemi et al. [44]. The sandstone

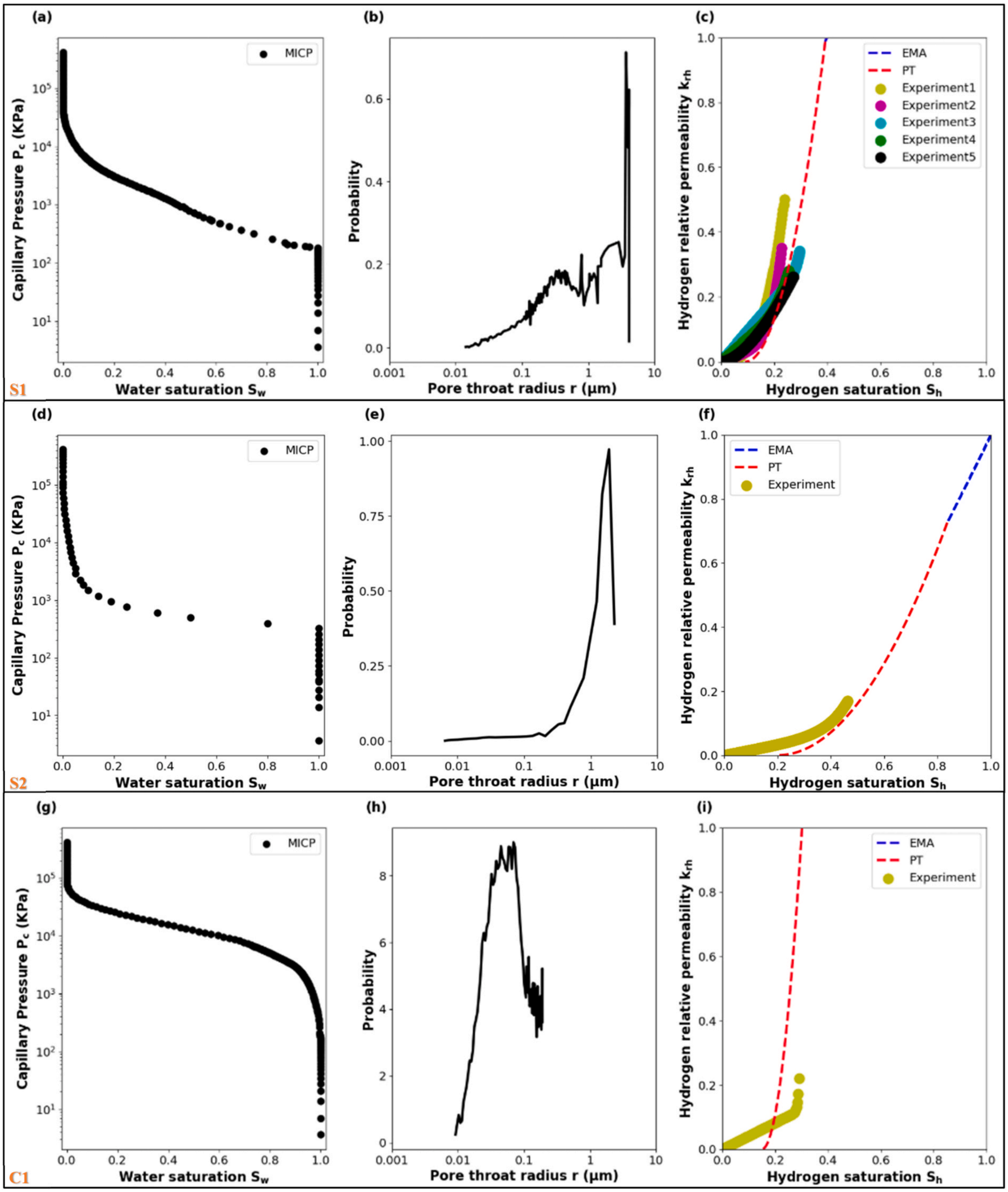

Fig. 2. (Left) CPCs (a, d and g), (middle) PSDs (b, e and h), and (right) estimated and measured hydrogen relative permeability curves (c, f and i) for the S1 sandstone sample (top). S2 sandstone sample (middle) and the C1 carbonate sample (bottom). Experimental data are from Rezaei et al. [45].

samples exhibited similar pore space characteristics (see PSDs shown in Fig. 6b, 6e and 6h), and resulted in similar S_{hc} values ($0.2 \le S_{hc} \le 0.25$; Table 2). Similarly, the carbonate samples had similar PSDs with pore sizes spanning from 1 to around 10 μm (Fig. 6k and 6n). As shown in Fig. 6c, 6f and 6i, the proposed model based on the PT and EMA estimated the k_{rh} accurately for the sandstones. We also found that although the sandstones have similar PSDs and S_{hc}, S_{hx} varies from 0.68 to 0.91. For the Berea* sandstone sample, a notable amount of residual water saturation was observed. As shown in Fig. 6f, the k_{rh} reaches 1 at $S_h = 0.76$, indicating that approximately 24 % of the pore space remains occupied by immobile water, which is not accessible to hydrogen flow.

Our k_{rh} estimations, however, are less accurate for the carbonate samples (Fig. 6i and 6o) [50]. Note that the scaling reduced to PT only (shown in red) for both carbonate samples. The PSDs of the sandstone samples (Fig. 6b, 6e and 6h) have similar broadness to those of the carbonate samples (Fig. 6k and 6n). However, the amount of water trapped is more significant in the carbonate samples than that in the sandstone samples suggesting the PSD contributing to hydrogen flow in the carbonate samples are practically narrower than those in the sandstone samples.

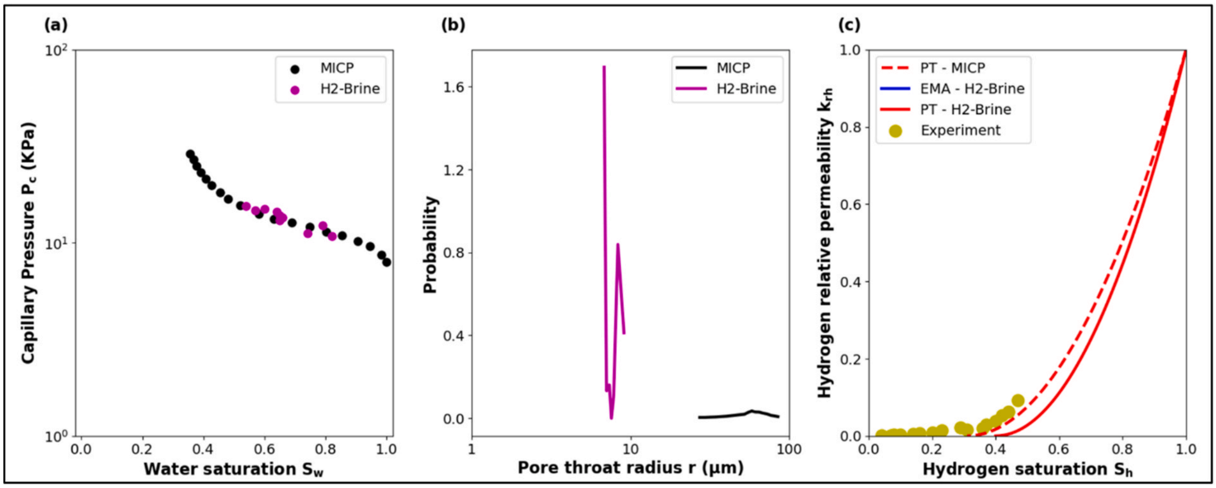

Fig. 3. (Left) CPCs (a), (middle) PSDs (b), and (right) estimated and measured hydrogen relative permeability curves (c) for the Berea (Liver) sandstone sample. Experimental data are from Boon and Hajibeygi [14].

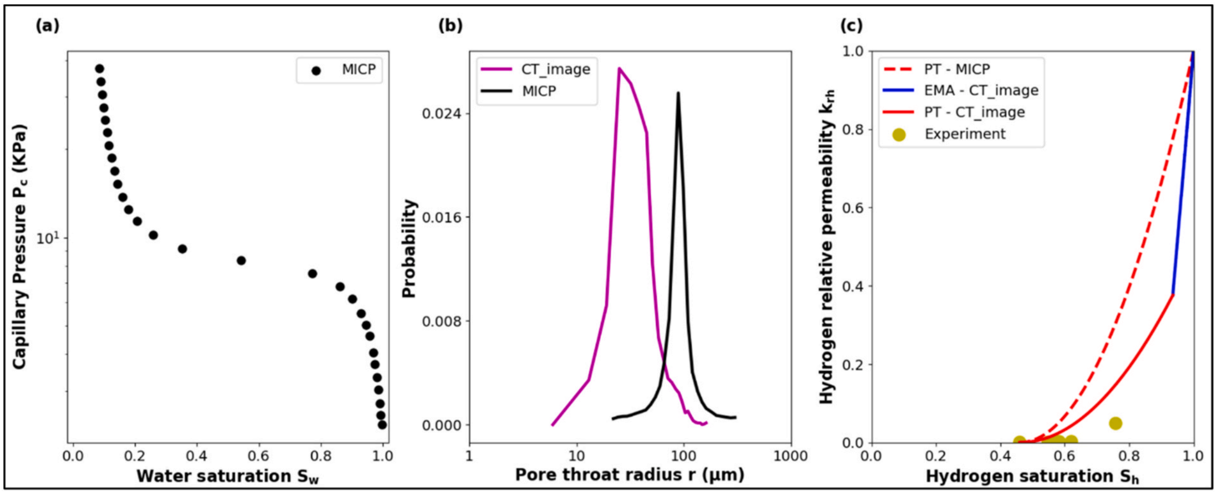

Fig. 4. (Left) CPC (a), (middle) PSDs (b), and (right) estimated and measured hydrogen relative permeability curves (c) for the Bentheimer sandstone sample. Experimental data are from Higgs et al. [15].

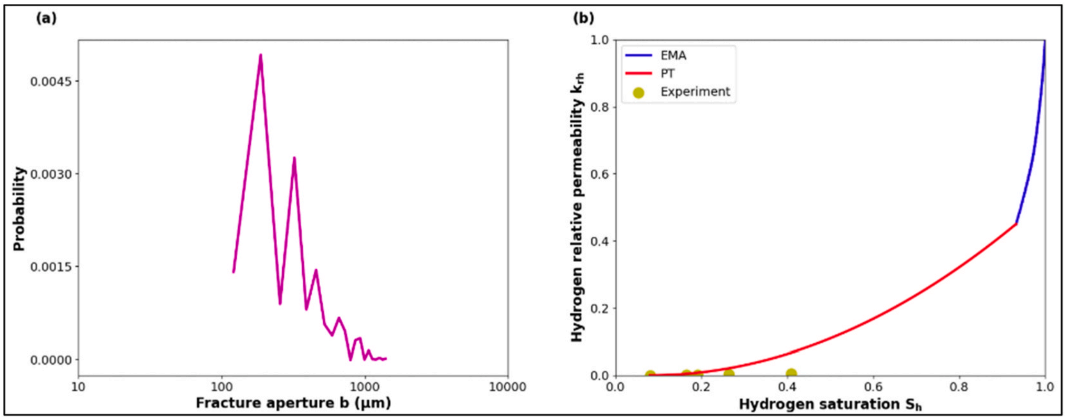

Fig. 5. (Left) Fracture aperture distribution (a), and (right) estimated and measured hydrogen relative permeability curve (b) for fractured carbonate samples. Experimental data are from Manoorkar et al. [16].

Fig. 7a–c presents the CPCs, PSDs, and k_{rh} curves for the sandstone sample S1 with simulations conducted using small and large contact angles (26.3° and 35.8°) from Zhao et al. [46]. The CPCs, PSDs and k_{rh} obtained at the contact angles of 26.3° and 35.8° show only minor differences indicating that increasing the contact angle within this ranges did not substantially affect these characteristics. The estimated k_{rh}

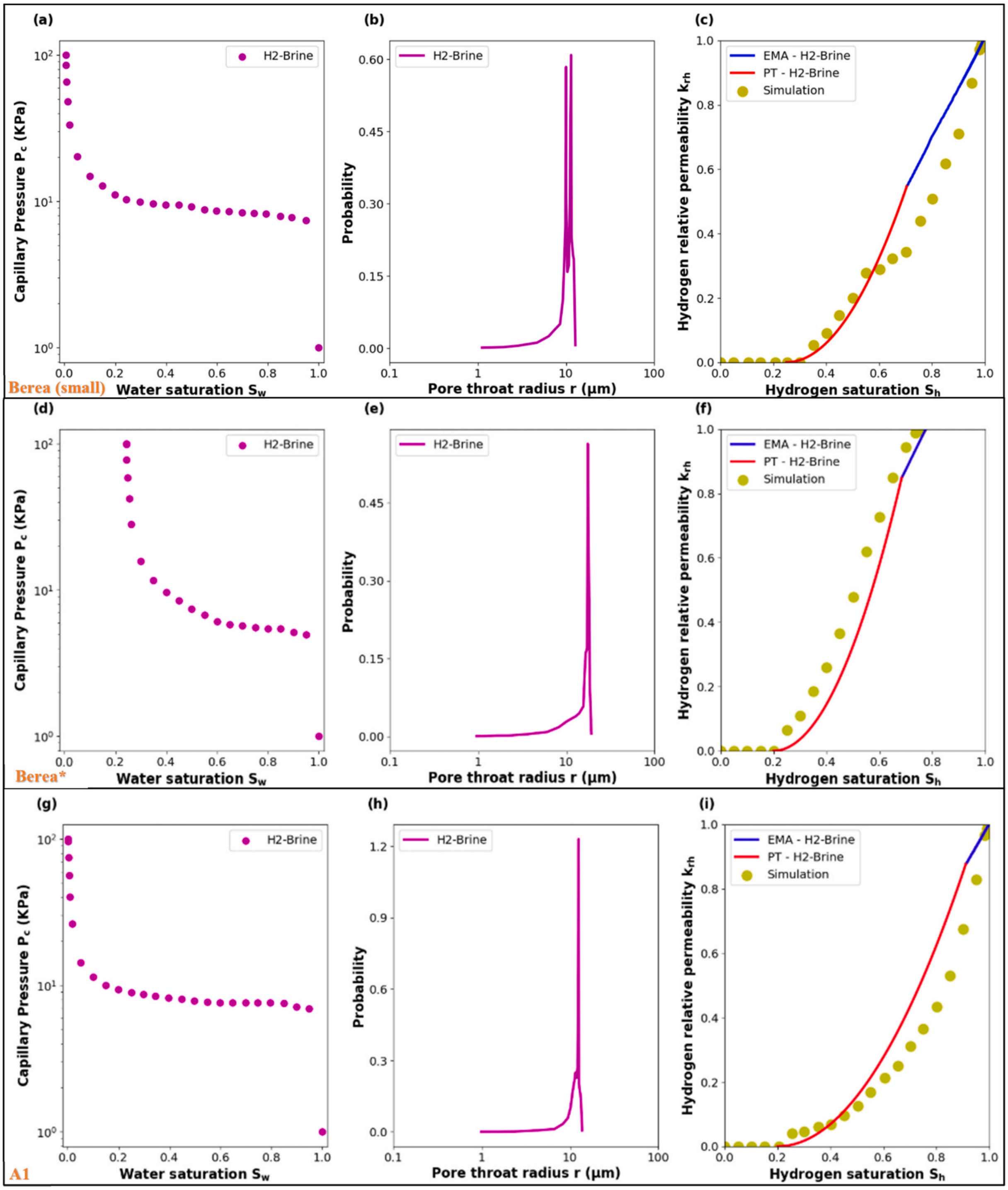

Fig. 6. CPC (a), PSD (b), and estimated and measured hydrogen relative permeability curves (c) for Berea (small) sandstone sample (first row). CPC (d), PSD (e), and estimated and measured hydrogen relative permeability curves (f) for Berea* sandstone sample (second row). CPC (g), derived PSD (h), estimated and measured hydrogen relative permeability curves (i) for A1 sandstone sample (third row). CPC (j), derived PSD (k), and estimated and measured hydrogen relative permeability curves (l) for C1 carbonate sample (fourth row). CPC (m), derived PSD (n), and estimated and measured hydrogen relative permeability curves (o) for C2 carbonate sample (fifth row). Numerical simulations are from Hashemi et al. [44].

matched the simulated one at high S_h but underestimated it at low and intermediate S_h values with $S_{hc} = 0.25$ (Table 2). The estimated S_{hc} is greater than the actual S_{hc} value near zero. Similar results were observed for the sandstone sample S7, as shown in Fig. 7l.

For the sandstone samples S2 and S3, the proposed model estimated k_{rh} accurately only at high S_h values, while at low S_h the model estimations do not agree well with the simulations (Fig. 7f and 7i). S_{hc} was underestimated for S2 and overestimated for S3. If one uses the data-derived S_{hc} values, reported in Table 2, more accurate estimations are obtained (results not shown). For the BG sandstone, the estimated $S_{hc} = 0.07$, determined from the inflection point of the MICP curve, agrees well with the data-derived S_{hc}, and led to accurate estimations of k_{rh}

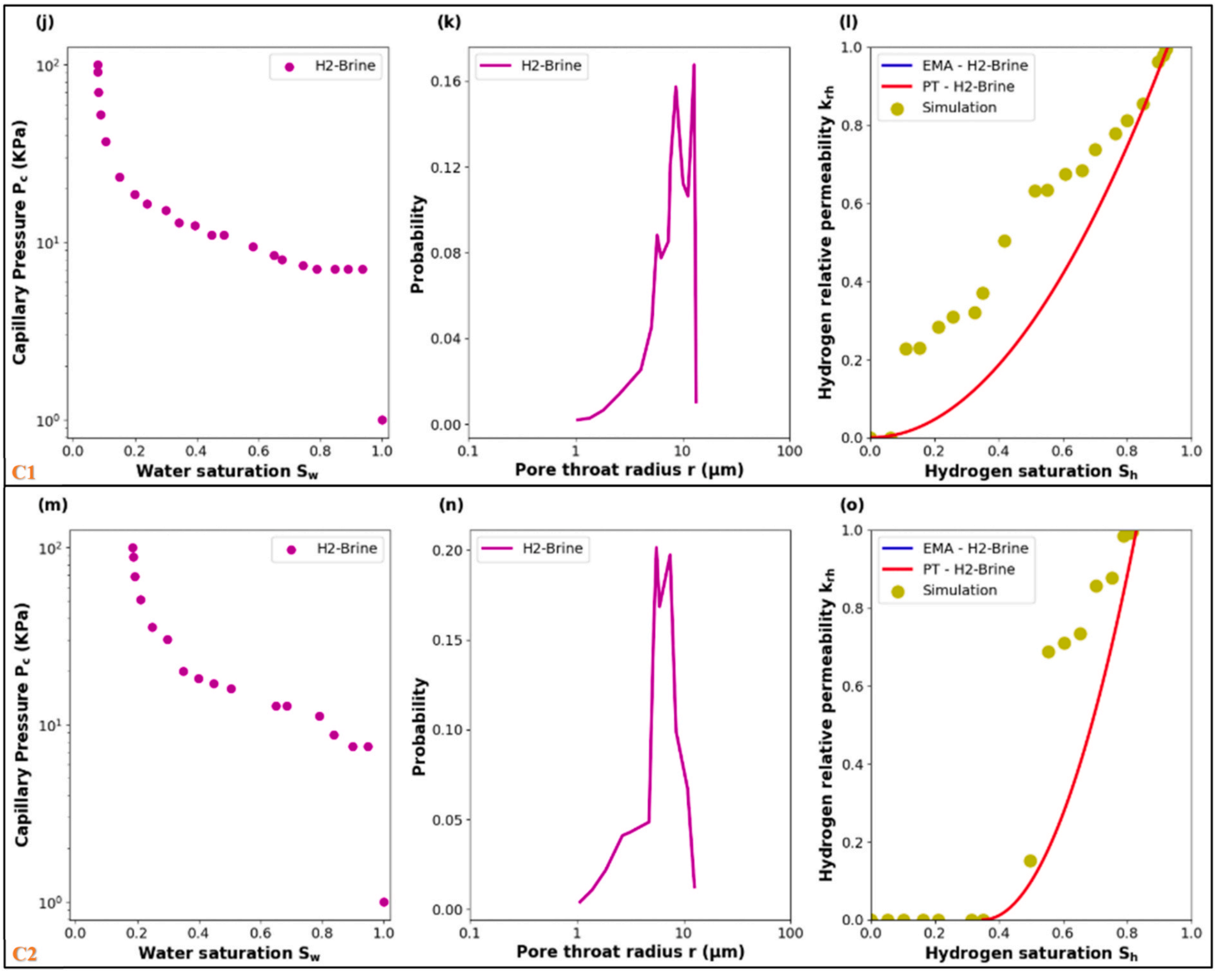

Fig. 6. (*continued*).

(Fig. 7o).

The PT scaling law appears to predominantly govern the flow behavior in samples S2, S3, and BG, whereas the remaining two samples exhibit a transition from the PT scaling to the EMA scaling over a significant range of hydrogen saturation.

5. Discussion

5.1. Primary drainage

Imbibition is generally more sensitive to wettability heterogeneity and therefore more complex to predict than drainage. Recently Nazari et al. [51] investigated the effects of wettability heterogeneity, reflected in uniform, random and correlated wettability distributions, on hydrogen displacement during drainage and imbibition by means of pore-scale simulations. They concluded that wettability effects have a pronounced influence during imbibition, while drainage is comparatively less affected despite exhibiting similar saturation levels. Nazari et al. [51] also reported that random wettability distributions decreased recovery efficiency, although correlated wettability linked to pore size promoted significant hydrogen trapping during imbibition.

In this study, we therefore used only the primary drainage data to evaluate our model. Secondary drainage and imbibition are associated with negative capillary pressures, which makes it difficult to (i) calculate $\Delta S_w/\Delta \ln(P_c)$, (ii) determine the pore radius r via the Young–Laplace equation (Eq. (1)), and (iii) derive the PSD from CPCs that include negative P_c values measured under primary imbibition and secondary drainage conditions. Nevertheless, even with the use of a single intrinsic contact angle and without explicitly representing wettability heterogeneity, our model demonstrates generally reasonable agreement with literature data for the primary drainage cases considered.

5.2. Critical hydrogen saturation S_{hc}

The critical hydrogen saturation is not a universal constant; rather, it is strongly influenced by the connectivity of pores, dimensions of a sample, and wettability characteristics [38]. Its precise estimation has been a longstanding issue in two-phase flow in porous media [33] and requires either accurate measurements of k_{rh} at low hydrogen saturations or comprehensive numerical simulations near the threshold, as stated earlier.

A consistent finding across datasets analyzed in this study was that the accuracy of k_{rh} estimations was highly sensitive to the choice of S_{hc}. In the sandstone cases (e.g., S1, S2, S3 and S7 samples from Zhao et al. [46]), the model produced good agreement at high hydrogen saturations but deviated at low S_h values when the estimated S_{hc} from the MICP or CPC differed from the data-derived values. Using data-derived S_{hc} values led to more accurate k_{rh} predictions, underscoring the importance of precise determination of this parameter. More so, for some carbonate and fractured samples, even small errors in S_{hc} led to more pronounced discrepancies, reflecting the greater sensitivity of complex pore structures to this threshold.

These results suggest that, in practice, S_{hc} should be constrained as tightly as possible, for example by extending capillary-pressure measurements to low gas saturations, combining complementary datasets (e.g., CPC and MICP or CT-based pore structure), or treating S_{hc} as a cali-

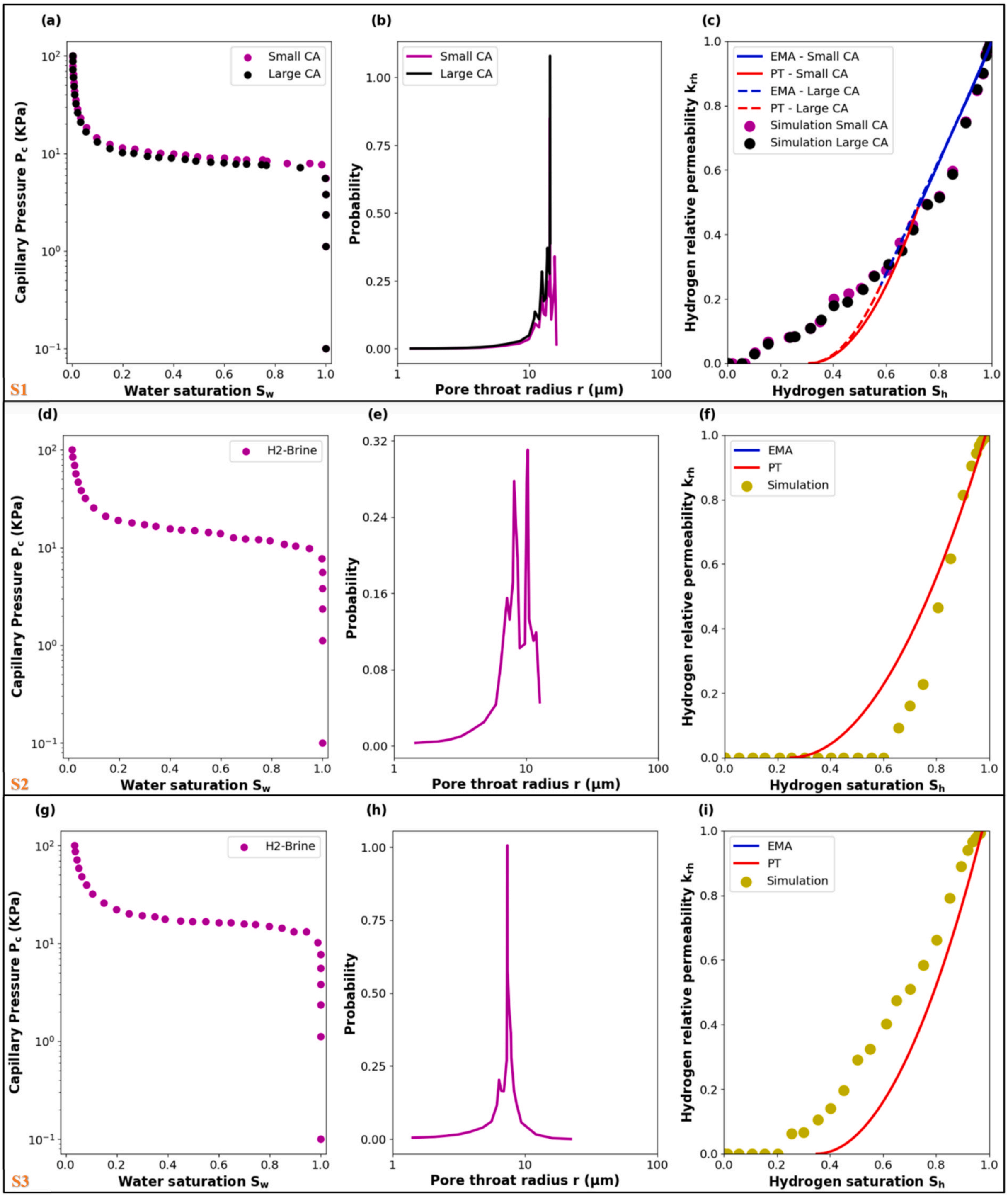

Fig. 7. CPC (a), derived PSDs (b), and estimated and measured hydrogen relative permeability curves (c) for the S1 sandstone sample using small and large contact angles (first row). CPC (d), derived PSD (e), and estimated and measured hydrogen relative permeability curves (f) for the S2 sandstone sample (second row). CPC (g), derived PSD (h), estimated and measured hydrogen relative permeability curves (i) for the S3 sandstone sample (third row). CPC (j), derived PSD (k), and estimated and measured hydrogen relative permeability curves (l) for the S7 sandstone sample (fourth row). CPC (m), derived PSD (n), and estimated and measured hydrogen relative permeability curves (o) for the BG sandstone sample (fifth row). Numerical simulations are from Zhao et al. [46].

bration parameter when both capillary pressure and relative permeability data are available.

5.3. Flow regimes: PT versus EMA

The relative importance of PT and EMA scaling was strongly dependent on PSD. Samples with narrow PSDs (approximately one order of magnitude) or small pore radii (mostly less than 10 μm) were predominantly governed by the PT scaling, consistent with significant water trapping and the dominance of percolation pathways (e.g., in Zhao et al. [46]'s S2, and S3, Rezaei et al. [45]'s S1 and C1, as well as the Berea sandstone). In contrast, samples with broader PSDs or larger pores

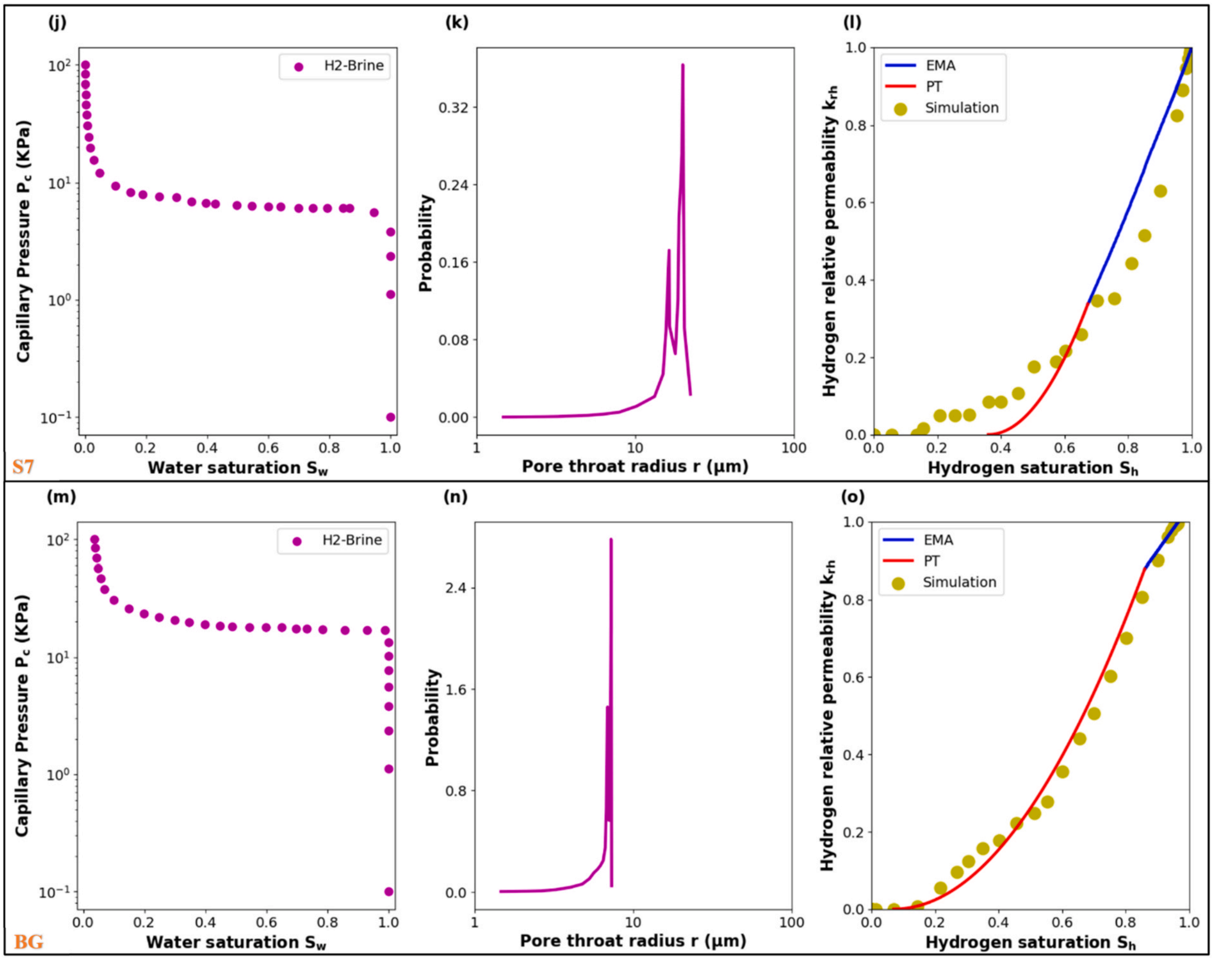

Fig. 7. (*continued*).

(though narrow PSDs) exhibited crossovers from PT to EMA scaling at hydrogen saturations ranging from 0.84 to 0.94 (e.g., Zhao et al.'s S1, S7, BG, Rezaei et al. [46]'s S2, Bentheimer sandstone, and the fractured carbonate sample from Manoorkar et al. [16]).

The above results also confirm the non-universality of the crossover saturation S_{hx} and highlight the sensitivity of flow regimes to subtle details in PSD geometry. Zhao et al. [46] compared cases with small differences in contact angle and showed that the resulting PSDs exhibited the same peak with only slight variations in width. The similarity in pore structure made the relative permeability curves largely consistent, although the crossover saturation (S_{hx}) differed. This suggests that even minor wettability variations may shift the transition between PT and EMA scaling without significantly altering the overall k_{rh} trend.

5.4. *Sandstones versus carbonates*

The sandstone samples generally exhibited better agreement between the estimated and measured or simulated k_{rh} compared to the carbonate rocks. In the sandstone cases (e.g., S1, S2, S3 and S7 from Zhao et al. [46], as well as the Berea sandstone from Boon and Hajibeygi [14] and the Bentheimer sandstone from Higgs et al. [15]), the predicted k_{rh} curves reproduced the overall trends of the reference data, with discrepancies mainly confined to low hydrogen saturations when S_{hc} was not accurately captured. In contrast, the carbonate samples (e.g., the C1, C2 (Fig. 6l and 6o) samples and the fractured carbonate from Manoorkar et al. [16]) displayed more pronounced discrepancies, particularly at intermediate hydrogen saturations, due to their complex pore systems involving vugs, microfractures, and dual-porosity features that may not be well captured by MICP or CPC alone. Therefore, modeling flow and transport in such rocks have been challenging [53]. In the fractured carbonate case (i.e., Manoorkar et al. [16]), however, accounting for fracture aperture distributions allowed the model to capture flow behavior reasonably better.

5.5. *Consistency and discrepancies between CPC- and MICP-derived* $\boldsymbol{k_{rh}}$ *curves*

As shown in Fig. 1c, the estimated k_{rh} curves are not greatly different, despite one was derived from the MICP curve and the other from the H_2-brine CPC (Fig. 1a). Comparable results were obtained across other datasets studied here. This consistency arises because the derived PSDs (Fig. 1b), while differing in range, exhibit comparable shapes and broadness. We found that shifting the PSD by multiplying pore sizes by a factor of 10 did not significantly alter the estimated k_{rh} (results not shown). This is due to the relative nature of k_{rh} in Eq. (8), where multiplying pore sizes by a constant factor proportionally increase both $k_h(S_h)$ in the numerator and $k_h(S_h = 1)$ in the denominator.

The PSD derived from the MICP captured larger pores while that obtained from the H_2-brine CPC captured smaller pores under both shallow- and deep-reservoir conditions. Due to practical limitations with sufficiently high pressures needed to penetrate very small pores in rocks, caution must be exercised when approaches, such as pressure measurements are applied to characterize pore space and its structure for UHS applications [52]. This is because pressure-based methods (e.g., MICP) may not fully capture the intricate interactions of hydrogen with pores, particularly small ones. The S_{hc} was determined from the inflection points of the H_2–brine CPC and MICP curve under both shallow and deep reservoir conditions, as reported in Table 2. While the S_{hc} values derived under the deep conditions were comparable across both methods, those under the shallow conditions showed noticeable discrepancies.

Fig. 1c and f displays the k_{rh} curves estimated from the MICP (dashed lines) and those from the H_2-brine CPC (solid lines). The difference between the estimations from the MICP and CPC is not substantial meaning that both approaches estimated the k_{rh} with more or less similar accuracy. For the deep-reservoir sample (Fig. 1f), however, the estimations from the H_2-brine CPC (solid line) are slightly more accurate than those from the MICP (dashed line).

The discrepancy between the estimated and measured k_{rh} curves (Fig. 1c and 1f) is likely due to the fact that our approach does not consider effects of pore and confining pressures [43]. It is also noteworthy that the flow behavior was predominantly governed by the PT scaling law, as the crossover point from the PT to EMA, $S_{hx} = 0.85$, occurred near the maximum S_h under both conditions.

5.6. *Comparison of methods (CPC, CT imaging)*

Our results showed method-dependent differences in the PSDs and k_{rh} estimations. For the Berea sandstone from Boon and Hajibeygi [14], the MICP approach tended to capture larger pores, while the micro CT-based method better characterized smaller pores. Zare Sourmanabad et al. [53] compared estimating wetting-phase relative permeability from CPC and PSD using 240 pore-network simulations and reported slightly more accurate predictions from the former (see their Fig. 6). Those authors attributed that to the fact that CPC probably captures dynamics of flow through pore space better than PSD. However, results from the Higgs et al. [15] dataset showed that micro CT gave a better prediction. We suspect the resolution of the image impacting modeling accuracy, however, one sample is not enough to make a conclusive discussion. Therefore, further investigation is required using more samples to compare estimating k_{rh} from CT images with that from MICP. Another observed difference between the two estimated k_{rh} curves is that the MICP-based curve (shown by dashed line in corresponding figures) is dominated by the PT scaling, while $S_{hx} = 0.94$ on the CT-based curve (thick line). This is because the PSD derived from MICP compared to that from CT-images seems to be narrower (Fig. 4b). These differences emphasize that choice of dataset can bias relative permeability predictions.

5.7. *Performance, controlling factors, and limitations of the* $\boldsymbol{k_{rh}}$ *estimations*

For sample S1 (Fig. 2c), the model underestimated k_{rh} curves at very low S_h values. This is because of the non-zero value of S_{hc} (=0.09), estimated from the inflection point of the MICP curve, which is greater than the data-derived $S_{hc} = 0.0015$ (Table 1). One would obtain more accurate estimations using $S_{hc} = 0.0015$. However, we do not show such results, simply because our aim was estimating the k_{rh} from the CPC or MICP without using the measured or simulated k_{rh} data. For the S2 sample, one would obtain even more accurate estimations (results not shown) using the data-derived $S_{hc} = 0.009$, reported in Table 2.

For C1 carbonate sample, the significant higher capillary pressures at high water saturations suggest that smaller pores dominated the sample. This is further supported by the distribution of pore-throat radii (Fig. 2h), which peaks in the sub-micron range, indicating a prevalence of small pores. The measured k_{rh} for the C1 sample shown in Fig. 2i: it initially followed a diagonal trend and then transitioned abruptly into a near-vertical rise. This behavior suggests that hydrogen was gradually displacing water at lower hydrogen saturations ($S_h < 0.28$) but then reached a breakthrough point, where continuous gas pathways formed led to a sudden increase in k_{rh}. The discrepancy between the measured and estimated k_{rh} curves suggests that some critical flow dynamics and saturation effects were not fully captured by either MICP or the proposed theoretical model based on the PT and EMA. One possible explanation could be the presence of vugs and/or fractures in the sample, common in carbonate reservoir rocks, that may not necessarily be captured by MICP [39].

We should point out that the proposed theoretical model is applicable to porous media with dual-porosity structures. For example, theoretical estimations of k_{rh} can be improved by incorporating corrective factors tailored for carbonate reservoirs. However, that requires accurate capturing of pore space, vugs, and microfractures in such complex porous rocks.

Samples S1 and C1 (Fig. 2c and i) are predominantly governed by percolation-type flow, as evidenced by significant water trapping, which results in a very narrow range of pores available for hydrogen flow. In contrast, Sample S2 exhibits a crossover from the PT scaling to the EMA scaling at a hydrogen saturation of $S_{hx} = 0.84$, attributable to its broad pore-throat size distribution spanning nearly three orders of magnitude.

For the Berea sandstone sample from Boon and Hajibeygi [14], the narrowing of the PSD derived from the H_2–brine CPC is primarily attributed to the limited range of capillary pressures employed during the measurements (Fig. 3a). The estimated k_{rh} from the MICP is shown via the dashed line and gave better agreement with measured k_{rh} than that obtained from H_2–brine CPC, shown in thick continuous line. This is because the value of $S_{hc} = 0.31$ (Table 2), estimated from the inflection point of the MICP curve, was more suitable than $S_{hc} = 0.4$ (Table 2), estimated from the inflection point of the H_2–brine CPC, for estimating the k_{rh} accurately. The error associated with the estimation of S_{hc} from the H_2-brine CPC is most probably because of the limited range of water saturation measured (Fig. 3a). Fig. 3c also shows that the flow behavior was completely governed by the PT scaling throughout the entire range of saturation. This is due to the narrow range of pore sizes observed in the PSDs (Fig. 3b).

For the fractured carbonate sample from Manoorkar et al. [16], the very low matrix porosity (less than 0.01) indicates that fluid transport is significantly influenced by the fracture network rather than the matrix. The estimated k_{rh} curve agrees reasonably well with the measured one at low S_h values, and the PT scaling law appears to dominate the flow behavior with a crossover to the EMA scaling at $S_h = 0.93$.

Taken together, these observations show that our approach performs best when the inferred S_{hc} is close to the data-derived value and when the relevant pore-scale features (e.g., broad PSDs, fracture networks, or vuggy porosity) are adequately captured by the available measurements (MICP, CPC, or CT imaging). At the same time, the discrepancies observed for some carbonate samples highlight the limitations of representing such complex pore structures with the current PT–EMA framework.

5.8. *Limitations and implications*

The proposed theoretically-grounded and computationally-efficient model is rather general, estimating k_{rh} from PSD based on pore-scale characteristics. Similar to other upscaling models, it involves simplifications that may limit its accuracy under complex geological conditions. In particular, while the model effectively captures saturation-dependent permeability trends, it does not account for some key physical factors, such as mineralogical heterogeneity, wettability variation, surface roughness, and the presence of vugs or fractures. These features, common in carbonates and fractured rocks, can significantly alter flow paths and contribute to discrepancies between model predictions and experimental data. As we stated earlier, the proposed theoretical k_{rh} model also does not consider effects of pore and confining pressures. In its current form, the model is formulated only for the hydrogen (non-wetting) phase and does not provide water relative permeability, which further limits its applicability for fully coupled two-phase flow simulations.

Moreover, the model assumes quasi-static, stable displacement and does not capture dynamic flow phenomena, such as viscous fingering, unfavorable mobility ratios, or capillary instabilities. It also neglects hysteresis, spatially variable wettability, confining pressure, and brine chemistry, which may be important under reservoir conditions. While these simplifications make the model analytically tractable, they limit its applicability in more complex systems. Further investigations are still required to address such limitations by incorporating pore-scale heterogeneity, wettability effects, dynamic displacement mechanisms and an explicit description of water relative permeability to improve the model robustness for real-world underground hydrogen storage applications.

6. Conclusions

In this study, we applied the concepts of the effective medium approximation (EMA) and universal power-law scaling from the percolation theory (PT) to develop a theoretical model for hydrogen relative permeability, k_{rh}, in potential reservoir rocks suitable for UHS. Our theoretical model calculates k_{rh} from the PSD and critical hydrogen saturation, S_{hc}. The latter was estimated from the inflection point of either MICP or H_2-brine CPC. To evaluate the proposed model, we compared theoretical estimations of k_{rh} with eight experiments and eleven simulations collected from the literature. Results showed that the k_{rh} was reasonably estimated for most of all the samples including experiments and simulations. However, we found predicting k_{rh} in carbonate rock samples challenging. This is because carbonate rocks may contain vuggy pore spaces and/or fractures, not necessarily captured by the MICP or CPC analyses. For two sandstone samples, we also found more accurate estimations, if the S_{hc} value was estimated more precisely. Our results showed the non-universality of the crossover hydrogen saturation S_{hx}, and suggested that the hydrogen flow behavior in most of the rocks aligns predominantly with the PT scaling. Further investigations are still required to incorporate the effects of other factors, such as the confining pressure, dual porosity, wettability variations and hysteresis, to improve the accuracy of k_{rh} estimations in UHS systems. The findings from this study demonstrate a proposed approach which provides a cost-effective and practical alternative to extensive experiments and simulations, offering a promising tool for quantifying k_{rh} relevant to UHS applications.

CRediT authorship contribution statement

Deborah O. Agbamu: Writing – review & editing, Writing – original draft, Visualization, Validation, Investigation, Formal analysis, Data curation, Conceptualization. **Qingqi Zhao:** Writing – review & editing, Writing – original draft, Validation, Methodology, Investigation, Data curation, Conceptualization. **Cheng Chen:** Writing – original draft, Validation, Supervision, Resources, Methodology, Investigation. **Hadi Hajibeygi:** Writing – original draft, Validation, Supervision, Resources, Methodology, Investigation. **Behzad Ghanbarian:** Writing – review & editing, Writing – original draft, Validation, Supervision, Resources, Methodology, Investigation, Data curation, Conceptualization.

Declaration of competing interest

The authors declare that they have no known competing financial interests or personal relationships that could have appeared to influence the work reported in this paper.

Acknowledgement

The authors thank Leila Hashemi (TNO) and Maartje Boon (University of Stuttgart) for sharing their data and for valuable discussions during this research. The authors also acknowledge the use of ChatGPT 3.5 for language editing and proofreading of this manuscript. The AI was used to improve grammar, clarity, and readability. All intellectual contributions, data interpretation, and conclusions remain the sole responsibility of the authors. D. A. is grateful to the geology Department, Kansas State University for financial supports through graduate teaching/research assistantships. B. G. acknowledges the University of Texas at Arlington for financial supports through faculty start-up fund and a STARs award.

Notations

$f(g)$	pore hydraulic conductance distribution
$f(r)$	pore size distribution
g	pore hydraulic conductance
g_e	effective pore conductance
g_{max}	maximum pore conductance
g_{min}	minimum pore conductance
k_0	numerical prefactor
k_h	hydrogen permeability
k_{rh}	hydrogen relative permeability
l	pore length
r	pore radius
r_{min}	minimum pore radius
r_{max}	maximum pore radius
S_h	hydrogen saturation
S_{hc}	critical hydrogen saturation
S_{hr}	residual hydrogen saturation
S_{hx}	crossover hydrogen saturation
S_w	water saturation
S_{winf}	water saturation corresponding to the inflection point
t	universal scaling exponent
μ	viscosity
γ	interfacial tension
θ	contact angle

References

[1] Dopffel N, Jansen S, Gerritse J. Microbial side effects of underground hydrogen storage – knowledge gaps, risks and opportunities for successful implementation. Int J Hydrogen Energy 2021;46:8594–606. https://doi.org/10.1016/j.ijhydene.2020.12.058.

[2] Winkler-Goldstein R, Rastetter A. Power to gas: the final breakthrough for the hydrogen economy? Green, 3; 2013. p. 69–78. https://doi.org/10.1515/green-2013-0001.

[3] Akpasi SO, Smarte Anekwe IM, Tetteh EK, Amune UO, Mustapha SI, Kiambi SL. Hydrogen as a clean energy carrier: advancements, challenges, and its role in a sustainable energy future. Clean Energy 2025;9:52–88. https://doi.org/10.1093/ce/zkae112.

[4] Sebastian S, Wijewardane S, Srinivasan S. Recent advances in hydrogen production, storage, and fuel cell technologies with an emphasis on inventions, innovations, and commercialization. Solar Compass 2023;8:100065. https://doi.org/10.1016/J.SOLCOM.2023.100065.

[5] Nong G, Li Y, Yin Y. Energy analysis on the water cycle consisting of photo catalyzing water splitting and hydrogen reacting with oxygen in a hydrogen fuel cell. Chem Phys Lett 2019;737:100033. https://doi.org/10.1016/J.CPLETX.2019.100033.

[6] Zivar D, Kumar S, Foroozesh J. Underground hydrogen storage: a comprehensive review. Int J Hydrogen Energy 2021;46:23436–62. https://doi.org/10.1016/j.ijhydene.2020.08.138.

[7] Raza A, Arif M, Glatz G, Mahmoud M, Al Kobaisi M, Alafnan S, et al. A holistic overview of underground hydrogen storage: influencing factors, current understanding, and outlook. Fuel 2022;330:125636. https://doi.org/10.1016/J.FUEL.2022.125636.

[8] Iglauer S, Ali M, Keshavarz A. Hydrogen wettability of sandstone reservoirs: implications for hydrogen geo-storage. Geophys Res Lett 2021;48. https://doi.org/10.1029/2020GL090814.

[9] Sambo C, Dudun A, Samuel SA, Esenenjor P, Muhammed NS, Haq B. A review on worldwide underground hydrogen storage operating and potential fields. Int J Hydrogen Energy 2022;47:22840–80. https://doi.org/10.1016/j.ijhydene.2022.05.126.

[10] Bo Z, Boon M, Hajibeygi H, Hurter S. Impact of experimentally measured relative permeability hysteresis on reservoir-scale performance of underground hydrogen storage (UHS). Int J Hydrogen Energy 2023;48:13527–42. https://doi.org/10.1016/j.ijhydene.2022.12.270.

[11] Kanaani M, Sedaee B, Asadian-Pakfar M. Role of cushion gas on underground hydrogen storage in depleted oil reservoirs. J Energy Storage 2022;45:103783. https://doi.org/10.1016/j.est.2021.103783.

[12] Lysyy M, Fernø M, Ersland G. Seasonal hydrogen storage in a depleted oil and gas field. Int J Hydrogen Energy 2021;46:25160–74. https://doi.org/10.1016/j.ijhydene.2021.05.030.

[13] Wang G, Pickup G, Sorbie K, Mackay E. Scaling analysis of hydrogen flow with carbon dioxide cushion gas in subsurface heterogeneous porous media. Int J Hydrogen Energy 2022;47:1752–64. https://doi.org/10.1016/j.ijhydene.2021.10.224.

[14] Boon M, Hajibeygi H. Experimental characterization of H 2/water multiphase flow in heterogeneous sandstone rock at the core scale relevant for underground hydrogen storage (UHS). Sci Rep 2022;12. https://doi.org/10.1038/s41598-022-18759-8.

[15] Higgs S, Wang Y Da, Sun C, Ennis-King J, Jackson SJ, Armstrong RT, et al. Direct measurement of hydrogen relative permeability hysteresis for underground hydrogen storage. Int J Hydrogen Energy 2024;50:524–41. https://doi.org/10.1016/j.ijhydene.2023.07.270.

[16] Manoorkar S, Pakkaner GK, Omar H, Barbaix S, Ceursters D, Lathinis M, et al. From underground natural gas to hydrogen storage in fractured reservoir rock : comparing relative permeabilities for hydrogen versus methane and nitrogen. 2024.

[17] Bagheri M, Mahani H, Ayatollahi S, Zivar D. Direct numerical approach for determination of H2-water flow functions applicable to underground hydrogen storage and production. J Energy Storage 2024;96:112573. https://doi.org/10.1016/J.EST.2024.112573.

[18] Krevor SCM, Pini R, Zuo L, Benson SM. Relative permeability and trapping of CO2 and water in sandstone rocks at reservoir conditions. Water Resour Res 2012;48. https://doi.org/10.1029/2011WR010859.

[19] Lenhard RJ, Parker JC, Mishra S. Measurement and prediction of saturation-pressure relationships in three-phase porous media systems. J Contam Hydrol 1987.

[20] Corey AT. The interrelation between gas and oil relative permeabilities. Prod Mon 1954;19:38–41.

[21] Brooks R, Corey A. Hydraulic properties of porous media. Hydrology 1964:27. Paper No 3.

[22] Brooks RH, Corey AT. Properties of porous media affecting fluid flow. J Irrigat Drain Div 1966;92:61–88.

[23] Li K. Analytical derivation of brooks-corey type capillary pressure models using fractal geometry and evaluation of rock heterogeneity. J Pet Sci Eng 2010;73:20–6. https://doi.org/10.1016/j.petrol.2010.05.002.

[24] Honarpour MM, Koederitz L, Harvey AH. Relative permeability of petroleum reservoirs. Boca Raton, FL: CRC Press; 1986.

[25] Van Genuchten M. A closed-form equation for predicting the hydraulic conductivity of unsaturated soils. Soil Sci Soc Am J 1980;44(5):892–8.

[26] Mualem Y. A new model for predicting the hydraulic conductivity of unsaturated porous media. Water Resour Res 1976;12:513–22.

[27] Ghanbarian B, Liang F, Liu HH, editors. Physics of fluid flow and transport in unconventional reservoir rocks. John Wiley & Sons; 2023.

[28] Lenhard RJ, Parker JC, Mishra S. On the correspondence between Brooks-Corey and van Genuchten models. J Irrigat Drain Eng 1991;117:610–1. https://doi.org/10.1061/(ASCE)0733-9437(1991)117:4(610.2.

[29] Parker JC, Lenhard RJ, Kuppusamy T. A parametric model for constitutive properties governing multiphase flow, 23. Porous Media; 1987.

[30] Ogolo NA, Ezeaneche OS, Onyekonwu MO. The comparison of experimental relative permeability data with Corey's model results: a case Study. Journal of Oil, Gas and Petrochemical Technology 2023;10:25–34. https://doi.org/10.22034/jogpt.2023.355385.1106.

[31] Sahimi M. Applications of percolation theory. second ed. Springer; 2023.

[32] Hunt A, Ewing R, Ghanbarian B. Percolation theory for flow in porous media, 880. Springer; 2014 (Vol. 880). Springer.

[33] Hunt A, Sahimi M. Flow, transport, and reaction in porous media: percolation scaling, critical-path analysis, and effective medium approximation. Rev Geophys 2017;55:993–1078.

[34] Heiba AA, Sahimi M, Scriven LE, Davis HT. Percolation theory of two-phase relative permeability. SPE Reserv Eng 1992;7:123–32.

[35] Levine S, Cuthiell DL. Relative permeabilitties in two-phase flow through porous media: an application of effective medium theory. J Can Petrol Technol 1986;25. https://doi.org/10.2118/86-05-10.

[36] Salimi H, Bruining J, Joekar-Niasar V. Comparison of modified effective-medium approximation to pore-network theory for relative permeabilities. J Pet Sci Eng 2020;184:106594.

[37] Ghanbarian B, Sahimi M, Daigle H. Modeling relative permeability of water in soil: application of effective-medium approximation and percolation theory. Water Resour Res 2016;52:5025–40. https://doi.org/10.1002/2015WR017903.

[38] Ghanbarian B, Liang F, Liu HH. Modeling gas relative permeability in shales and tight porous rocks. Fuel 2020;272. https://doi.org/10.1016/j.fuel.2020.117686.

[39] Ghanbarian B, Javadpour F. Upscaling pore pressure-dependent gas permeability in shales. J Geophys Res Solid Earth 2017;122:2541–52. https://doi.org/10.1002/2016JB013846.

[40] Richesson S, Sahimi M. Hertz-Mindlin theory of contacting grains and the effective-medium approximation for the permeability of deforming porous media. Geophys Res Lett 2019;46:8039–45. https://doi.org/10.1029/2019GL083727.

[41] Sahimi M. Flow and transport in porous media and fractured rock. Wiley; 2011. https://doi.org/10.1002/9783527636693.

[42] Agbamu D, Zhao Q, Chen C, Hajibeygi H, Ghanbarian B. Python code for estimating hydrogen relative permeability from capillary pressure curve, Mercury intrusion porosimetry curve or pore-throat size distribution. http://www.hydroshare.org/resource/5434f8d66a9e475896fb8cfe215db768; 2025.

[43] Yekta AE, Manceau JC, Gaboreau S, Pichavant M, Audigane P. Determination of hydrogen–water relative permeability and capillary pressure in sandstone: application to underground hydrogen injection in sedimentary formations. Transport Porous Media 2018;122:333–56. https://doi.org/10.1007/s11242-018-1004-7.

[44] Hashemi L, Blunt M, Hajibeygi H. Pore-scale modelling and sensitivity analyses of hydrogen-brine multiphase flow in geological porous media. Sci Rep 2021;11. https://doi.org/10.1038/s41598-021-87490-7.

[45] Rezaei A, Hassanpouryouzband A, Molnar I, Derikvand Z, Haszeldine RS, Edlmann K. Relative permeability of hydrogen and aqueous brines in sandstones and carbonates at reservoir conditions. Geophys Res Lett 2022;49. https://doi.org/10.1029/2022GL099433.

[46] Zhao Q, Wang H, Chen C. Underground hydrogen storage: a recovery prediction using pore network modeling and machine learning. Fuel 2024;357. https://doi.org/10.1016/j.fuel.2023.130051.

[47] Ni H, Boon M, Garing C, Benson SM. Predicting CO2 residual trapping ability based on experimental petrophysical properties for different sandstone types. Int J Greenh Gas Control 2019;86:158–76. https://doi.org/10.1016/j.ijggc.2019.04.024.

[48] Fredlund DG, Xing A. Equations for the soil-water characteristic curve, 31; 1994.

[49] Witherspoon PA, Wang JS, Iwai K, Gale JE. Validity of cubic law for fluid flow in a deformable rock fracture. Water Resour Res 1980;16:1016–24.

[50] Shapiro AM. The challenge of interpreting environmental tracer concentrations in fractured rock and carbonate aquifers. Hydrogeol J 2011;19:9–12.

[51] Nazari M, Mahani H, Ayatollahi S. Pore-scale insights on mixed-wettability and its impact on underground hydrogen storage in aquifers. Adv Water Resour 2025;204:105044. https://doi.org/10.1016/J.ADVWATRES.2025.105044.

[52] Peng S, Zhang T, Loucks RG, Shultz J. Application of Mercury injection capillary pressure to mudrocks: conformance and compression corrections. Mar Petrol Geol 2017;88:30–40. https://doi.org/10.1016/J.MARPETGEO.2017.08.006.

[53] Zare Sourmanabad M, Norouzi S, Mirzaei F, Yokeley BA, Ebrahimian H, Ghanbarian B. A percolation model of unsaturated hydraulic conductivity using three-parameter Weibull distribution. Adv Water Resour 2024;188. https://doi.org/10.1016/j.advwatres.2024.104696.

[54] Kirkpatrick S. Classical transport in disordered media: scaling and effective-medium theories. Phys Rev Lett 1971;27(25):1722–5.

[55] Ghanbarian-Alavijeh B, Hunt AG. Comparison of the predictions of universal scaling of the saturation dependence of the air permeability with experiment. Water Resour Res 2012;48(8):W08513.